Active Spectral Imaging

Melissa L. Nischan, Rose M. Joseph, Justin C. Libby, and John P. Kerekes

With the ability to image a scene in tens to hundreds of spectral bands, multispectral and hyperspectral imaging sensors have become powerful tools for remote sensing. However, spectral imaging systems that operate at visible through near-infrared wavelengths typically rely on solar illumination. This reliance gives rise to a number of limitations, particularly with regard to military applications. Actively illuminating the scene of interest offers a way to address these limitations while providing additional advantages. We have been exploring the benefits of using active illumination with spectral imaging systems for a variety of applications. Our laboratory setup includes multispectral and hyperspectral sensors that are used in conjunction with several laser illumination sources, including a broadband white-light laser. We have applied active spectral imaging to the detection of various types of military targets, such as inert land mines and camouflage paints and fabrics, using a combination of spectral reflectance, fluorescence, and polarization measurements. The sensor systems have been operated under a variety of conditions, both in the laboratory and outdoors, during the day and at night. Laboratory and outdoor tests have shown that using an active illumination source can improve target-detection performance while reducing false-alarm rates for both multispectral and hyperspectral imagers.

Multispectral and hyperspectral imaging systems, operated from ground-, airborne-, and space-based platforms, have found a variety of civilian and military applications. This technology has applications in fields that range from environmental monitoring and geology to mapping, military surveillance, and reconnaissance. The power of multispectral and hyperspectral imaging arises from the ability to image a scene rapidly in tens to hundreds of spectral bands. The spectral signatures acquired in this fashion make it possible to discriminate among different types of materials.

Operating at visible through shortwave infrared wavelengths (0.4 μm to 2.5 μm), passive multispectral and hyperspectral imaging systems measure reflected solar radiation. The radiance measured at the sensor represents a combination of the solar spectrum, the atmospheric absorption along the path from the sun to the scene to the sensor, the inherent reflectance properties of objects in the scene, the illumination geometry, and the sensor system characteristics. For many applications, this dependence on the conditions under which measurements are made can complicate analysis, making it difficult, if not impossible, to compare spectral data taken under different conditions. In these cases, it becomes important to convert the data from radiance units (measured at the sensor) to reflectance units (an inherent property of a material). The reflectance spectrum of an object is determined by its physical composition, and provides a fingerprint that can be used for material classification and identification.

The utility of reflectance spectra is ultimately determined by the accuracy of the data conversion from radiance to reflectance units and the conditions under which measurements are made. For example, changes in the angles between the sun, target, and imaging system can affect the reflectance, and also introduce shadowing within a scene. In shadowed regions, the illumination may differ in both amplitude and spec-

tral shape from areas that are directly lit. Variations in spectral illumination in a scene increase the uncertainty in the derived reflectance spectra, making material identification more difficult and false alarms more common.

An active spectral imaging system has the potential to alleviate the aforementioned problems as well as offer additional benefits. Placing the illumination source on the sensor platform provides a constant angle between the source, target, and sensor. This geometry eliminates illumination-angle variations that can complicate analysis and degrade performance. Laboratory and outdoor tests have shown that using an active source also drastically reduces shadowing, which reduces false-alarm rates. Moreover, active illumination enables a sensor to operate day or night, even under adverse weather conditions when solar illumination is greatly reduced. If the illumination source is pulsed, photons reflected from an intervening obscurant between the sensor and the target (e.g., a tree canopy or camouflage netting) can be removed through time gating. Discrimination capabilities can be further enhanced through the addition of polarization and fluorescence measurements. Using an active source with a known output polarization simplifies measurement of polarization signatures, which can be used to distinguish man-made from natural materials. And when the appropriate stimulation wavelengths are used, laser illumination can be used to induce chlorophyll fluorescence, a vegetation marker.

Laser illumination in a sensor system is not a new concept. A coherent laser radar that uses a carbon dioxide (CO_2) laser was developed in 1967 [1]. Other early proposed applications of laser illumination include improving signal-to-noise ratio, mitigating backscatter from intervening atmosphere, and obtaining relative target reflectance [2]. More recently, semiconductor and microchip lasers have played a key role in the development of three-dimensional imaging laser radar (ladar) systems [3]. The active spectral imaging program at Lincoln Laboratory has been exploring the benefits of combining laser and laser-like illumination with compact hyperspectral and multispectral imagers. The program initially focused on phenomenology associated with hyperspectral detection of targets and backgrounds when using active illumination [4]. We studied targets with relevance to military applications, such as inert land mines and various camouflage materials and paints. Subsequently, we expanded our investigations to include active multispectral imaging and conducted a series of laboratory and outdoor tests to demonstrate detection of concealed targets in natural backgrounds. The remainder of this article describes our equipment, laboratory setup, analysis techniques, and results of laboratory and outdoor measurements.

Equipment and Laboratory Setup

We assembled a pair of sensor systems for hyperspectral and multispectral imaging in the visible and near-infrared (VNIR), ~0.4 μm to 1 μm, and shortwave infrared (SWIR), ~1 μm to 2.5 μm, wavelength regions. The VNIR and SWIR hyperspectral systems were developed for laboratory-based phenomenological studies, providing images with high spatial and spectral resolution. Both hyperspectral systems can be converted to multispectral by simply changing the means of spectral dispersion. The multispectral imagers, with their compact size and a coarser spectral resolution that increases the data-collection rate, are more suited for outdoor measurements than are the hyperspectral imagers.

Each of the systems can be used with or without an active-illumination source. The choice of illumination source depends on the application. For phenomenological investigation that requires high-resolution spectral measurements, a white-light laser is used for illumination. This compact laser source, developed at Lincoln Laboratory [5], generates broadband spectral illumination (532 nm to ~850 nm) while retaining the high-brightness, subnanosecond-length pulse characteristics of its pump laser. (Additional information on this laser can be found in the sidebar entitled "White-Light Laser.") For fluorescence and polarization imaging, the higher-power single-frequency (532 nm) output of the pump laser is used directly. Results from phenomenological measurements made in the SWIR indicate an interesting anomaly-detection technique that requires using just two spectral bands [6]. On the basis of these results, we obtained 1410-nm and 1600-nm continuous wave (CW) lasers, each with 500-mW output power.

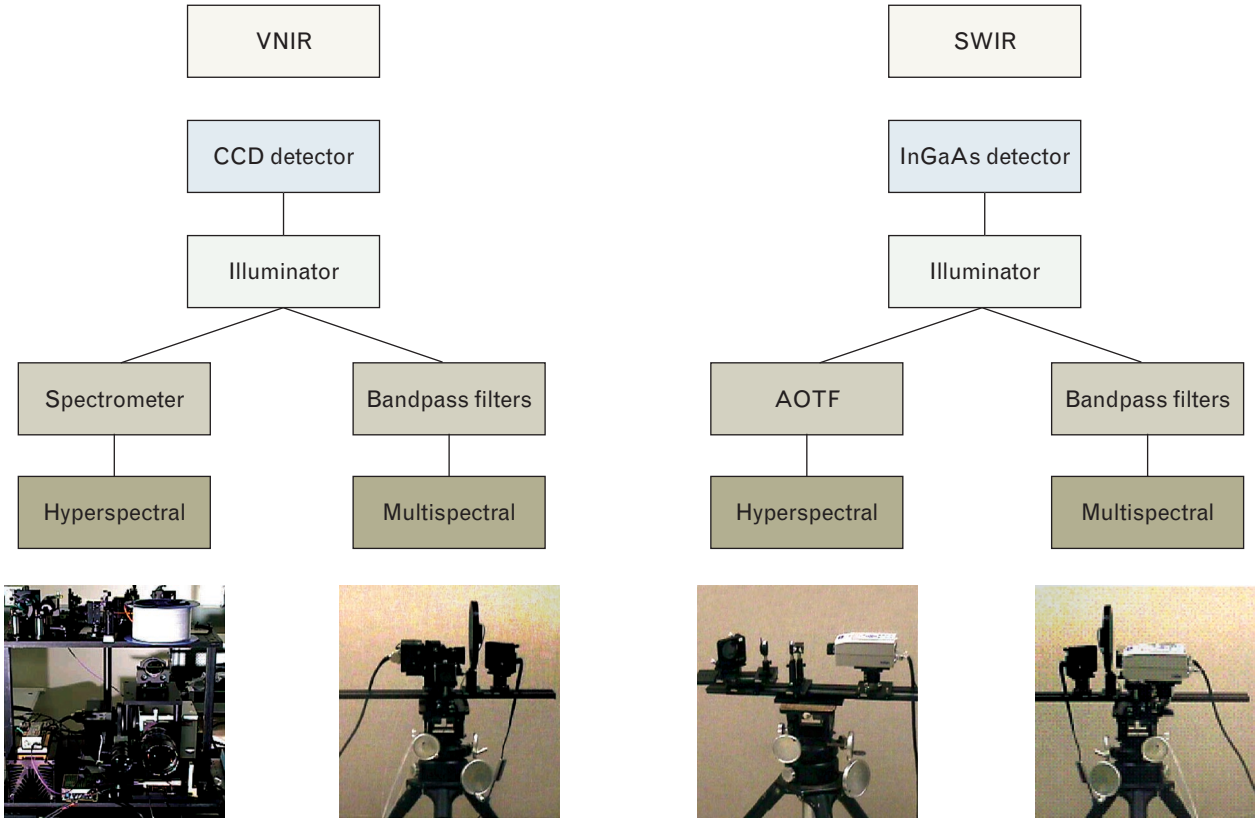

FIGURE 1. Four possible spectral imaging system configurations: visible and near-infrared (VNIR) hyperspectral, VNIR multispectral, shortwave infrared (SWIR) hyperspectral, and SWIR multispectral. The hyperspectral systems were developed for laboratory-based phenomenological studies to provide images with high spatial and spectral resolution. Both hyperspectral systems can be converted to multispectral by simply changing the means of spectral dispersion. With the VNIR system, the spectrometer is replaced with a set of VNIR bandpass filters; with the SWIR system, the acousto-optic tunable filter (AOTF) is replaced by a set of SWIR bandpass filters. More than the hyperspectral systems, the multispectral systems are suitable for outdoor measurements because of their compact size and a coarser spectral resolution that increases the data-collection rate. Separate detectors must be used for the VNIR and SWIR systems—a silicon charge-coupled device (CCD) focal-plane array and an indium gallium arsenide (InGaAs) focal-plane array, respectively.

Figure 1 illustrates how the individual components of each system can be combined to operate as either hyperspectral or multispectral imagers. The VNIR system uses a silicon charge-coupled device (CCD) focal-plane array, with either a grating-based slit spectrometer for hyperspectral measurements, or individual bandpass filters for multispectral measurements. (The center wavelength of the filters ranges from 400 nm to 950 nm in increments of 50 nm with ~40-nm spectral width.) The SWIR system uses an indium gallium arsenide (InGaAs) focal-plane array, with either an acousto-optical tunable filter (AOTF) for hyperspectral measurements, or individual bandpass filters for multispectral measurements. The AOTF has 10-nm spectral resolution with continuous coverage from 1.2 μm to 2 μm. Although the AOTF can be tuned over this entire range, the longest wavelength detectable by the InGaAs camera is 1.7 μm. The SWIR filters range from 1 μm to 1.9 μm with widths of 20 nm to 100 nm.

The output of a hyperspectral or multispectral imager can be thought of as a three-dimensional image cube with two spatial dimensions and one spectral dimension. Figure 2 shows an example of a hyperspectral image cube, in which each pixel in the two-dimensional array has an associated spectral signature that represents the spectral contributions from every object in the pixel. Because only two of the dimen-

WHITE-LIGHT LASER

THE WHITE-LIGHT LASER, developed at Lincoln Laboratory, is based on a 532-nm diode-pumped microlaser. The 532-nm microlaser, shown in Figure A, is pumped by a 3-W near-infrared (808 nm) diode laser coupled to the microlaser by 1 m of optical fiber. The microlaser is passively *Q*-switched to produce short pulses (~400 psec) at high repetition rates, up to 16 kHz, with approximately 5 to 8 μJ of energy per pulse. The output from the 532-nm diode-pumped microlaser is focused into a single-mode silica fiber (core diameter ~6 μm) of approximately 100 m in length to generate the broadband output. Intensities greater than 10 GW/cm^2 are achieved in the fiber core, and within a few meters of propagation a Stokes-shifted stimulated Raman scattering (SRS) pulse is generated. This pulse, which occurs at 440 cm^{-1} from the 532-nm radiation, is spectrally broadened because of the inherently large Raman gain bandwidth (~40 THz) of silica fibers. This initial Stokes-shifted pulse induces a second-order SRS pulse, which is further spectrally broadened, that pumps the higher-order Stokes shifts. After eight to ten Raman shifts, the pulses are sufficiently broadened that they overlap to form a continuum. For fibers of ~100 m, the continuum extends from about 680 nm to 900 nm, as shown in Figure B. The energy conversion from the green 532-nm input to the broadband "white light" output is between 10 to 15%. The high repetition rate and short pulse structure of the input beam are preserved.

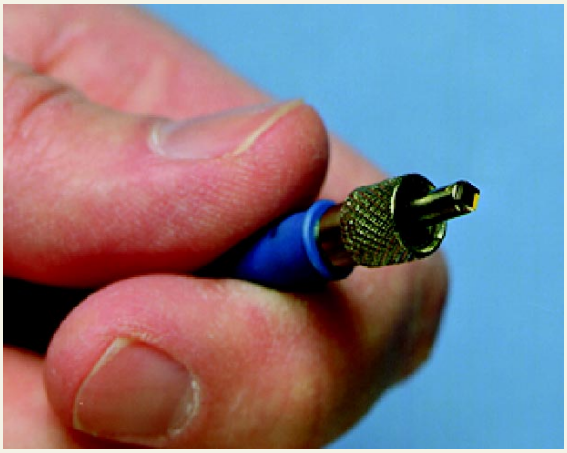

FIGURE A. Simplest embodiment of passively *Q*-switched microchip laser. The microchip laser is attached to the end of an optical fiber, through which it is pumped with an 808-nm diode laser.

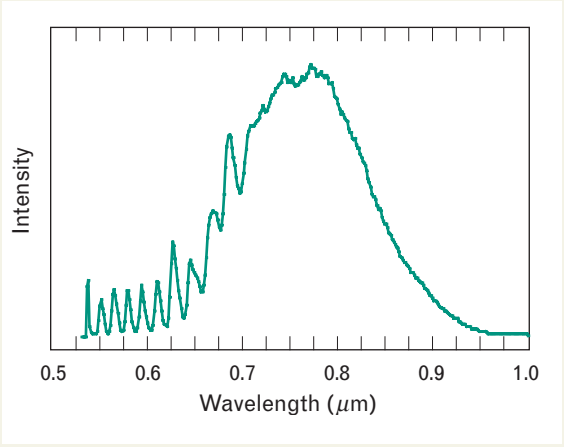

FIGURE B. White-light laser output spectrum. Individual Raman peaks start at 532 nm and broaden into a continuum by approximately 680 nm.

sions can be acquired at once, there are two different modes of operation possible. In the staring mode, the entire scene is imaged onto the focal plane, one spectral band at a time. In the scanning mode, the spectral dimension and one spatial dimension are imaged onto the focal plane, and the entire system is scanned spatially across the scene.

Only the VNIR hyperspectral system operates in a scanning mode, imaging a single vertical strip, one pixel wide, through a grating-based slit spectrometer,

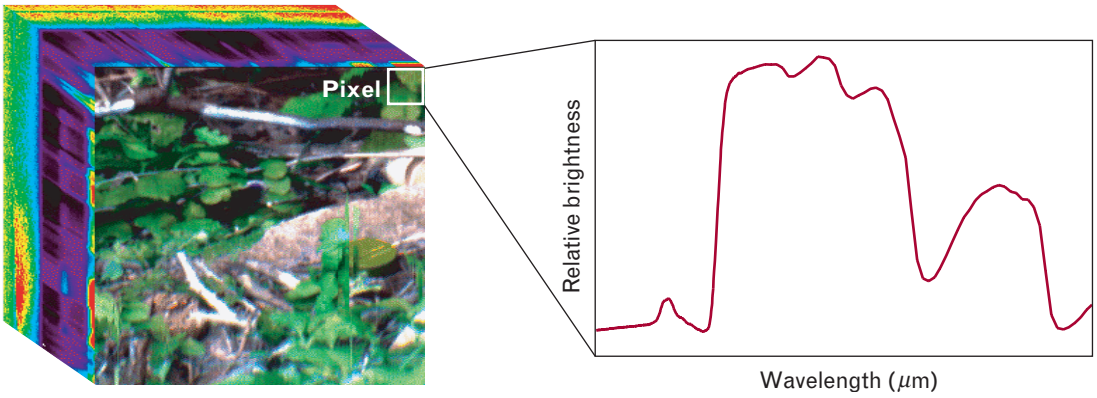

FIGURE 2. Example of a three-dimensional hyperspectral image cube. Two dimensions are spatial, and one spectral. Each pixel contains a spectrum that represents a combination of the spectral contributions from every object in the pixel.

as shown in Figure 3. The spectrometer disperses the light onto the CCD, such that one dimension represents spatial sampling and the second dimension represents spectral sampling. The whole setup is mounted on a tripod and scanned in azimuth across the scene to acquire the second spatial dimension, completing the image cube. The vertical entrance slit of the spectrometer determines the instantaneous field of view of the imager. Cylindrical optics are used to shape the outgoing laser beam to match the field of view of the imager.

Data Processing

Before the raw output of the sensor can be used, the data must be corrected for sensor-related effects. This initial preprocessing includes wavelength calibration and correction for detector nonuniformity, sensor artifacts, and background levels. After the data have been corrected, further analysis steps are determined by how the data will ultimately be used. For example, detecting and identifying specific materials or targets by using a reference spectrum requires high-resolution spectra plus conversion of the data to reflectance units to remove environmental and sensor effects. Removing these effects allows us to compare spectra taken under different conditions. In contrast, detecting anomalies or doing broad classification of the pixels in a scene can often be accomplished with lower-resolution spectra, and the data may not need to be converted to reflectance units.

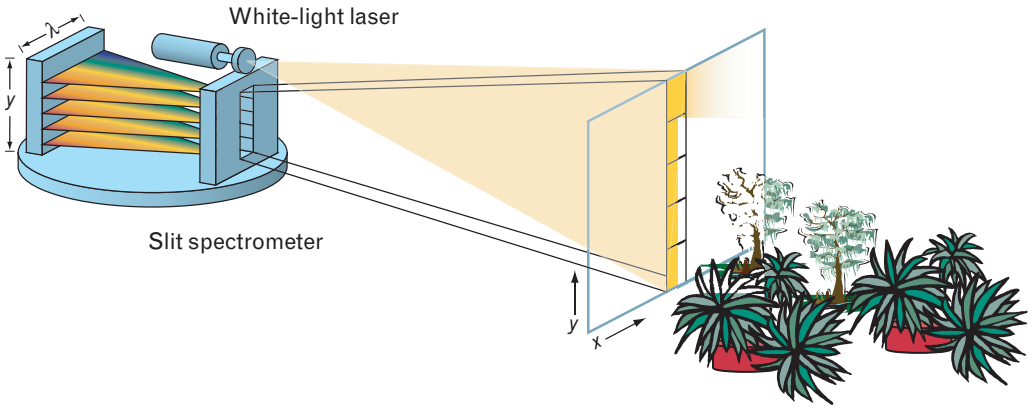

FIGURE 3. Operation of the VNIR hyperspectral imager. The system acquires a spectral signature for every pixel in the vertical slit field of view of the imager. The system is scanned in azimuth to build a three-dimensional hyperspectral image cube. The laser divergence is matched to the field of view of the imager.

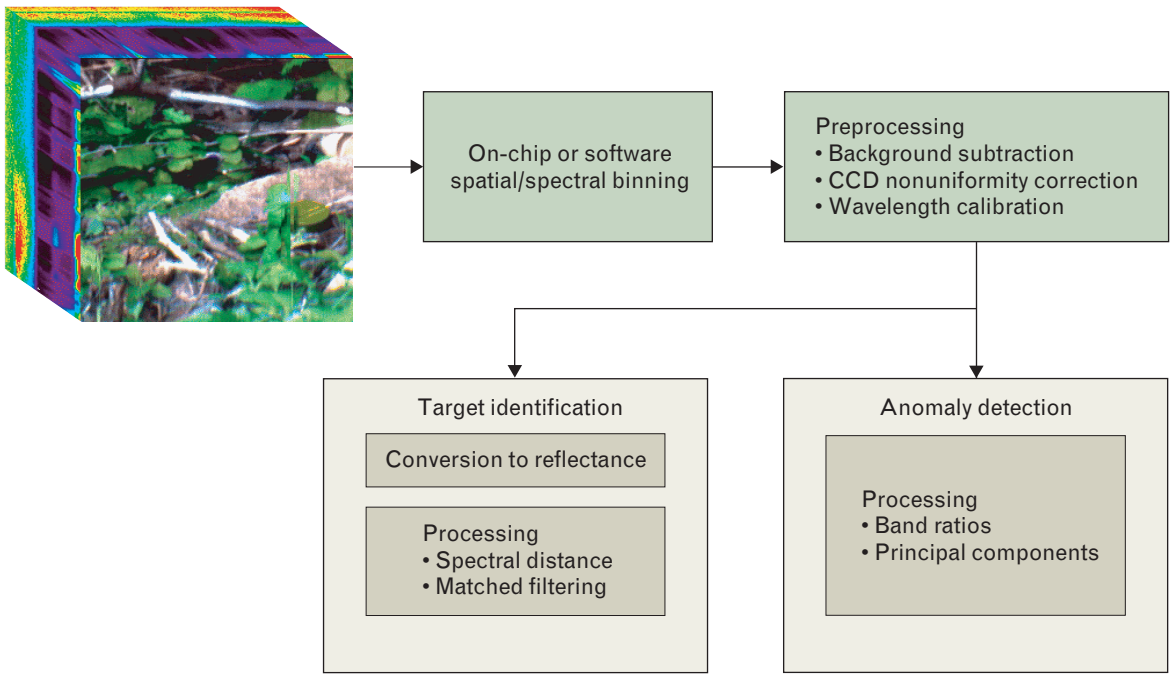

FIGURE 4. Hyperspectral/multispectral data processing procedure. Raw sensor data must first undergo a preprocessing step that includes calibration and correction. In our work, the next step is processing related to either target identification or anomaly detection. The target-identification processing begins with converting the data to reflectance units. Then we apply spectral distance or matched-filtering algorithms to identify targets. For anomaly detection, conversion to reflectance units is not a prerequisite. Spectral band ratios and principal-component analysis are two examples of anomaly-detection techniques that can be applied to the data.

In our experiments, the goal was usually target identification or anomaly detection. Figure 4 outlines the processing steps performed in each case. For target identification, the spectrum from each pixel in the data set is compared to a library of reflectance spectra for various target and background materials in an attempt to find the best match. Most of the library spectra we use were compiled from high-resolution scans of the targets taken in the laboratory, and some spectra were drawn from the Aster Spectral Library.*

Before a meaningful comparison between library and image spectra can be made, the image cubes are converted from radiance units to reflectance units by using one of many existing techniques. An extensive discussion of these methods is beyond the scope of this article, but numerous references can be found [7]. We used an in-scene calibration panel with known spectral characteristics as a reference to normalize the data. The calibration panel has a reflectance of almost 99% over the VNIR-SWIR spectral range and is a well-characterized, highly Lambertian scatterer. This technique has the advantages of being both accurate and easy to implement, and the disadvantage of being impractical to use in a noncooperative scenario.

Once the data have been converted to reflectance units, a variety of spectral detection algorithms can be used to find and identify targets in the scene [8]. Two of the algorithms that we use for processing are spectral angle map (SAM) and Euclidean minimum distance (EMD). These simple distance measures quantify the difference between a library reference spectrum and a measured spectrum by treating them as a vector in spectral space and calculating the cosine of the angle between them (in the case of SAM) or calculating the geometric distance between them (in the case of EMD). These detection methods are far

* The ASTER Spectral Library includes data from three other spectral libraries: the Johns Hopkins University Spectral Library, the Jet Propulsion Laboratory Spectral Library, and the United States Geological Survey Spectral Library. More information can be found at <http://speclib.jpl.nasa.gov>.

from optimal, but they are computationally efficient and they have reasonably good performance for our applications.

We use two approaches to anomaly detection. One approach involves detecting small, localized spectral anomalies, such as man-made objects, in an otherwise natural background. We search for a small number of pixels whose spectra differ from the local or the global background spectra. The second approach uses a distinguishing spectral feature in the target that enables detection with just a few spectral bands.

As a final step, the results of either target identification or anomaly detection can be combined with polarization and/or fluorescence measurements to enhance target-detection performance and reduce false-alarm rates.

Fusion of Hyperspectral, Polarization, and Fluorescence Data

In this section we demonstrate the benefit of combining polarization and fluorescence data with active hyperspectral data. These three types of measurements provide complementary information that can be combined to enhance detection performance and reduce false alarms.

A number of studies have demonstrated the use of polarimetry to detect man-made objects in a natural clutter background [9]. Polarimetry offers an additional discriminant because naturally occurring objects such as grass, soil, and other rough surfaces tend to depolarize incident light more than smoother man-made objects. Consequently, a scene imaged at orthogonal polarizations will show variations in the intensity of the detected light that depend on the relative smoothness of the objects in the scene.

There can be situations in which a natural background, such as a smooth, broad leaf plant, shows as much polarization as some man-made materials. In this case, laser-induced fluorescence imaging, used primarily to monitor vegetation for signs of stress and disease [10], allows us to discriminate between vegetative and non-vegetative materials. With this technique, a laser source excites chlorophyll fluorescence, which has spectral peaks at 685 nm and 740 nm.

To test the fusion of active hyperspectral, polarization, and fluorescence data, we constructed a target scene in the laboratory. Figure 5 shows a photo of the target scene, which contains an empty metal shell casing and three different types of plastic (similar to the plastics used in antipersonnel and antitank land mines). The scene was imaged by using the VNIR hyperspectral imager with the white-light laser for illumination. For the polarization measurement, the vertically polarized 532-nm pump laser illuminated the scene. A polarizer was placed in front of the detector, and the scene was imaged with the receive polarization both parallel and perpendicular to the outgoing beam. Then the polarizer was removed from the detector and a fluorescence measurement was taken, again by using the 532-nm laser for illumination.

FIGURE 5. Digital-camera photo of the target scene, containing soil, vegetation, rocks, sticks, three different types of plastic, and a metal shell casing.

Initial preprocessing of the hyperspectral data cube was performed as described earlier. We applied the SAM and EMD algorithms to detect the targets in the scene. A library of target spectra, including various plastics, metals, paints, and vegetation, had been collected earlier in separate measurements. These reference spectra served as inputs into the SAM and EMD algorithms, which worked effectively at detecting the plastics, but were not able to detect the metal shell casing, as shown in Figure 6. To detect the shell casing, we used the additional discrimination provided by the polarization and fluorescence data.

The two orthogonal polarization images were used to calculate the degree of polarization (DOP), which is a measure of the amount of polarization in the laser light reflected from objects in the scene. The DOP is

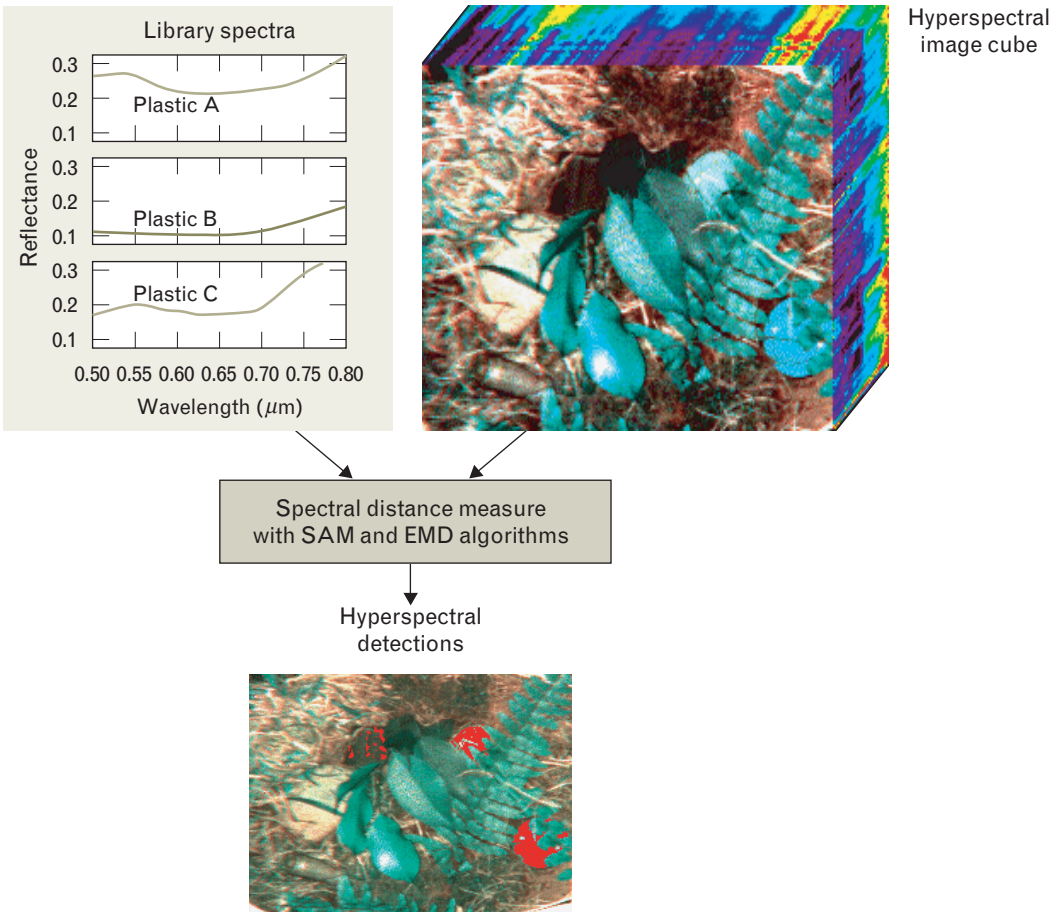

FIGURE 6. The hyperspectral image cube (upper right) processed by using library spectra with spectral angle map (SAM) and Euclidean minimum distance (EMD) algorithms, resulting in detection of the plastic, but not the metal, targets. Detections are indicated in red. Note that the color balance in the rendition of the hyperspectral image cube is skewed by the lack of blue wavelengths because the shortest wavelength in the white-light laser illumination is 532 nm (green).

the difference of the two orthogonal polarization measurements divided by their sum:

$$\mathrm{DOP} = \frac{I_{\|} - I_{\perp}}{I_{\|} + I_{\perp}},$$

where $I_{\|}$ is the parallel polarization component and $I_{\perp}$ is the perpendicular polarization component. Objects with smooth surfaces tend to have a higher DOP than objects with rough surfaces.

Figure 7 shows grayscale images of the target scene showing DOP and fluorescence imaging. Higher DOP values appear brighter and lower DOP values appear darker. Some of the smooth, flat leaves in the scene have a DOP as high as the metal targets, which indicates that polarization alone is unable to distinguish between the two materials. We used fluorescence imaging to highlight the vegetation in the scene and eliminate the false detections in the DOP detection of the metal shell casing. Figure 8 shows the detections, including the metal shell casing, that result from the fusion of the active hyperspectral, polarization, and fluorescence data.

Shadow Reduction

We live in a three-dimensional world, and three-dimensional objects cast shadows. Within the shadows, what little illumination exists is a combination of diffuse sky illumination and secondary scattering from nearby objects. Because the exact composition of the

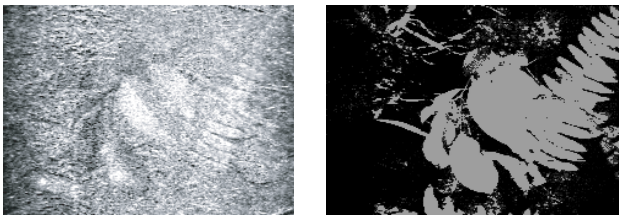

FIGURE 7. Degree of polarization of the target scene, left, and a corresponding fluorescence map, right. Note that some of the smooth, flat vegetation returns high polarization values, which could be interpreted as possible targets. Fluorescence imaging, which identifies vegetation, helps eliminate some of these possible targets.

shadow illumination is unknown, the retrieved reflectance spectra from shadow regions are unreliable. Shadow regions are a problem for passive sensors because the illumination and viewing angles are almost always different, which results in shadows in the scene. By using an illumination source at the sensor platform, we can force the illumination and viewing geometries to be the same. This arrangement greatly reduces shadows, which increases the visibility of targets and decreases the false-alarm rate [11].

To demonstrate the effects of shadow reduction, we acquired a hyperspectral image cube of the scene pictured in Figure 5, first using ambient illumination (fluorescent room lights) and then using active illumination with the white-light laser.* Figure 9 shows grayscale single-band (572 nm) images taken under ambient and active illumination. Although the shadow regions in the ambient image have three times the amount of light as the same regions in the active image, the circular shapes of plastics A and B are more discernible in the active image. This effect, seen across all spectral bands, occurs because the active illumination source is aligned with the detector, allowing more direct light to reach the targets, which in turn reduces shadows and increases visibility.

To quantify the benefits of shadow reduction, we used the SAM algorithm to find and identify the two plastic mine-like objects (plastics A and B in Figure 5) in both the ambient and active data sets. Spectral angles between each pixel in the two data sets and the

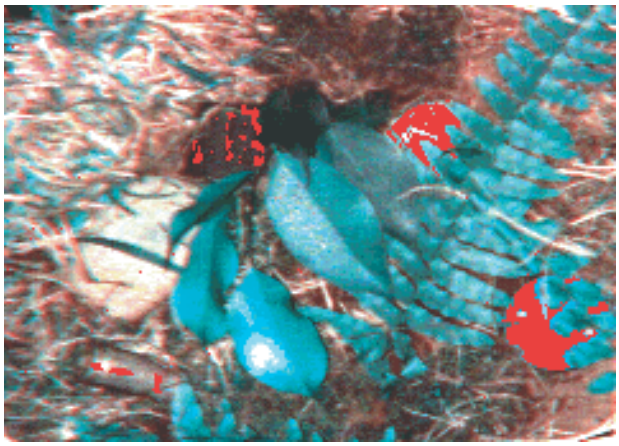

FIGURE 8. Detections, in red, of the plastic and metal targets. Fusion of the spectral-reflectance, polarization, and fluorescence data allows us to detect the metal shell casing (bottom left), which we could not detect with active hyperspectral data alone.

library spectra were calculated. The resulting spectral angle maps were then compared to a truth map that indicated which pixels in the scene consisted entirely of plastic A or plastic B. A spectral angle threshold was set for each target such that 60% of the target pixels were correctly identified. With these thresholds, we calculated false-alarm rates on a per-pixel basis for each data set and target. This procedure was then repeated on both data sets for varying levels of spectral resolution. Lower spectral resolution was simulated by binning adjacent bands to achieve the desired spectral bandwidth.

Figure 10 compares the false-alarm rates for the active and ambient data sets for varying spectral resolutions. For both targets, the false-alarm rates for the active image cube are significantly lower than those of the ambient image cube by as much as two orders of

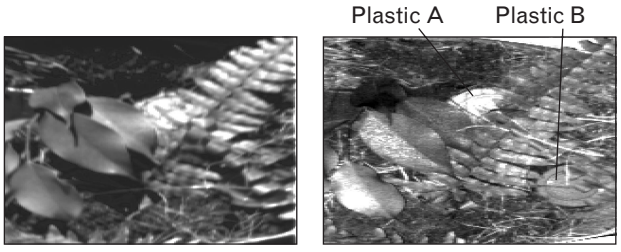

FIGURE 9. Ambient (left) and active (right) images taken at 572 nm. Notice the increased contrast in the actively illuminated image

* We refer to data taken under ambient illumination as the ambient data, and to data taken under active illumination as the active data.

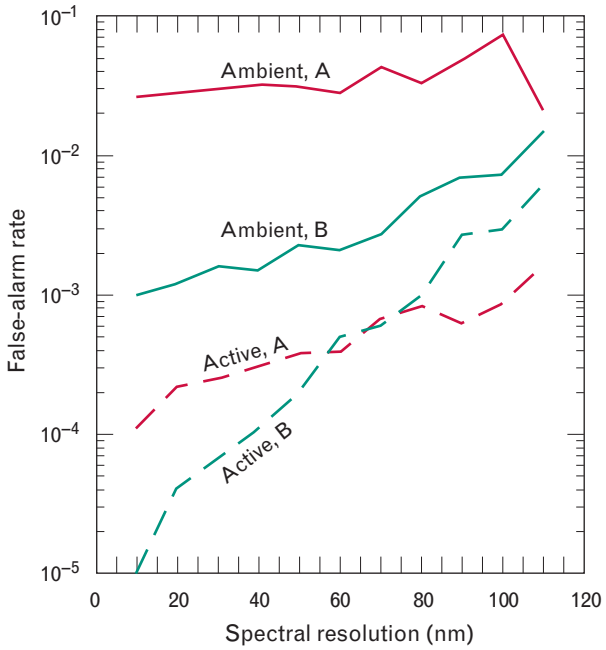

FIGURE 10. Per-pixel false-alarm rate for detecting mine-like objects (plastics A and B) in the scene from Figure 5. The use of active illumination reduced the false-alarm rate by about two orders of magnitude.

magnitude. This improvement is entirely due to shadow reduction. The lower false-alarm rate for active illumination holds even as the spectral resolution of the data is degraded. It appears that for plastic B, the false-alarm difference between the active and ambient images gets smaller as spectral resolution degrades. This effect is an artifact of the white-light laser spectrum. Spectral binning of data taken with the white-light laser involves binning over successive Raman peaks (see Figure B in the sidebar entitled "White-Light Laser"). The phase of the spectral bin with respect to the Raman peaks changes the signal-to-noise ratio of the binned data, causing the apparent false-alarm convergence for ambient and active data as spectral resolution decreases. Even under these non-ideal conditions, false-alarm rates for the active data are significantly lower than those of the ambient data.

We note that the false-alarm rates quoted here are quite high. Because the image contains about 10^5 pixels, a false-alarm rate of 10^{-4} indicates about 10 false alarms in this scene. However, no spatial processing has been performed to reduce the false-alarm rate, and requiring 60% of the visible target pixels to fall within our "detection" threshold is a relatively strict requirement.

SWIR Anomaly Detection

In a related study, we have discovered that water-vapor absorption lines in the SWIR are exploitable sources of contrast that enable us to distinguish between natural and man-made objects [5]. Man-made objects, particularly paints and plastics, tend to be hydrophobic; they are designed to repel water to prevent rust, corrosion, and degradation. Natural materials, on the other hand, tend to be hydrophilic; they retain water because they are either porous (in the case of rocks and soils), or living (in the case of vegetation). Consequently, natural objects like rocks and foliage typically absorb more radiation in the 1.4-μm and 1.9-μm water-vapor absorption lines than do man-made objects. By taking a simple ratio of two broad SWIR spectral bands, one within a water-vapor absorption line and one outside a water-vapor absorption line, we can achieve good anomaly-detection performance and distinguish man-made objects from natural objects.

We performed an outdoor experiment using surface-scattered inert land mines to test this anomaly-detection technique. Five mines and a calibration panel were placed in a scene that contained natural clutter such as grass, rocks, sticks, and plants, as shown in Figure 11. The scene was imaged with and without active illumination at a range of 20 m. The active illumination was provided by a pair of lasers operating at 1410 nm and 1600 nm. Three of the mines in the scene were positioned such that when active illumination was not used, they were either partially or completely shadowed by plants and rocks. The other two mines were completely exposed.

Figure 12 shows a simple band ratio (dividing one image by the other on a pixel-by-pixel basis) of the 1410-nm image to the 1600-nm image for the scene taken with and without active illumination. Man-made materials tend to have larger band-ratio values (brighter pixels in the image), while natural materials tend to have smaller band-ratio values (darker pixels in the image). A band-ratio threshold value was chosen such that at least one pixel on each of the targets

FIGURE 11. Photograph of the imaged scene comprising five inert land mines amidst clutter of rocks, sticks, and vegetation. White circles indicate target positions and the black square indicates the position of the calibration panel.

was detected. The pixels in each image exceeding the threshold are denoted in yellow. While the targets are detectable by using this two-band technique without active illumination, the number of false alarms in the actively illuminated scene is clearly lower. In Figure 13 a horizontal profile taken across the position of one of the mines illustrates the difference in contrast between the two data sets.

We explored this reduction in false alarms by examining the cumulative probability distributions of the band-ratio values in the targets and in the background. The first step in calculating the distributions was subtracting a wide area (20 × 20 pixels) median-filtered version of the band-ratio image from itself to eliminate a gradient across the scene that was caused by variations in the spatial illumination pattern of the two lasers. The distribution of the background pixels was then calculated from all the pixels in the band-ratio image, excluding the targets and the calibration panel. The target distributions were calculated separately for each target.

Figure 14 shows the cumulative probability distributions of band-ratio values for the scene imaged first without active illumination and then imaged with active illumination. By looking at these cumulative probability distributions, we can compare the percentage of target pixels exceeding the band-ratio threshold (detections) to the percentage of background pixels exceeding the band-ratio threshold (false alarms). For example, suppose we want to set a band-ratio threshold value for each scene such that we detect at least 60% of the pixels on each target. For

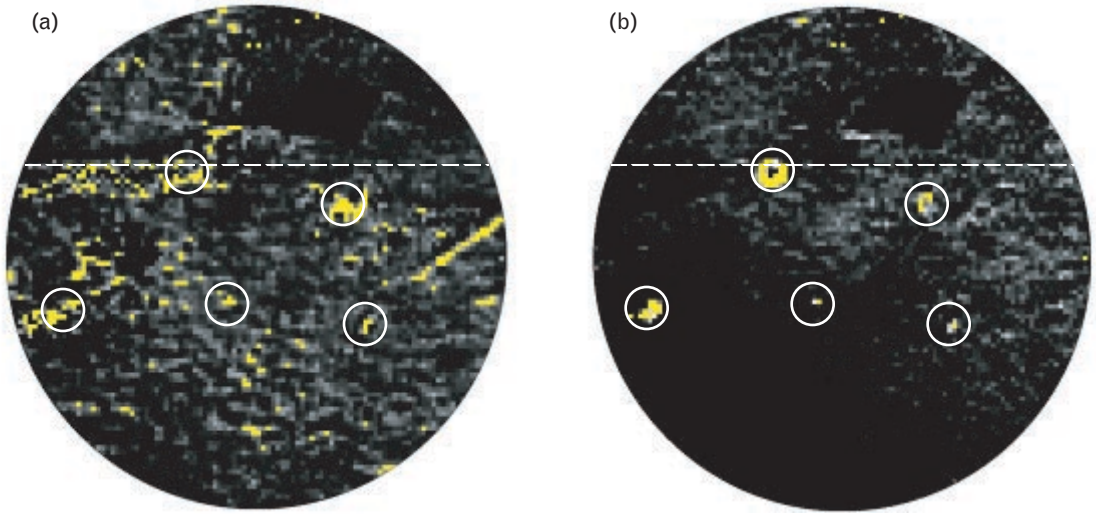

FIGURE 12. 1410-nm/1600-nm band ratios, using data taken (a) without active illumination and (b) with active illumination. Circles indicate target positions. Yellow pixels have values that exceed the band-ratio threshold. The positions of the horizontal profiles shown in Figure 13 are indicated by a dashed white horizontal line on the band-ratio images.

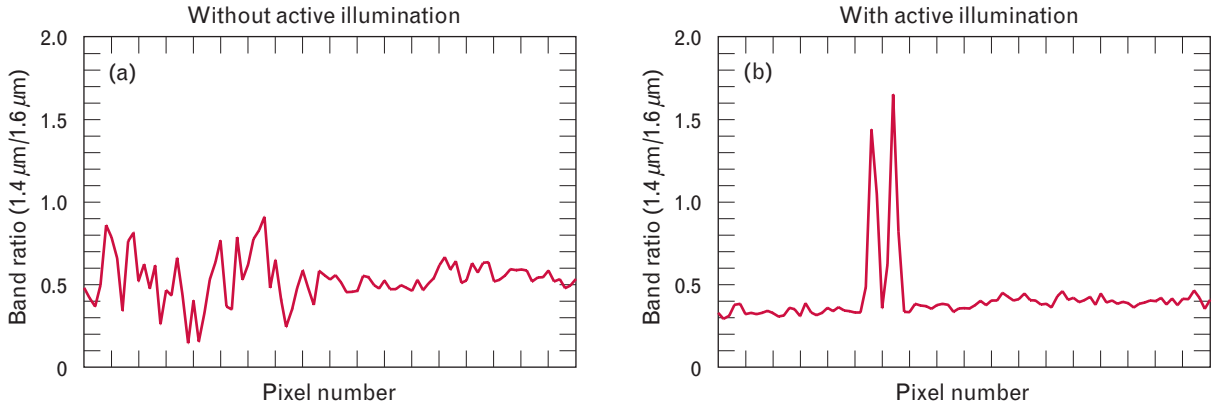

FIGURE 13. Horizontal profiles taken across the same vertical position (indicated by dashed white lines in the band-ratio images shown in Figure 12) taken (a) without active illumination and (b) with active illumination. The central portion of the mine across which the profiles are taken is made of a material different from the outer portion. The dip in ratio values seen in (b) may be caused by a spectral feature present in the mine's inner material but not present in its outer material.

the scene imaged without active illumination, this constraint leads to a band-ratio threshold of 0.15, as indicated by the dashed gray vertical line in Figure 14(a). At this threshold, 6% of the background pixels exceed the threshold and are considered false alarms. For the actively illuminated scene, the band-ratio threshold necessary to detect at least 60% of the pixels on each target is 0.13, which corresponds to only 0.1% of the background pixels exceeding the threshold, an improvement factor of 60.

It is important to note that these numbers are conservative estimates. Our targets ranged in size from 280 cm^2 down to 25 cm^2. For the smallest mines, given the resolution of our camera, we had only about 4 pixels on target. The odds of each target pixel falling exactly within a pixel on the sensor were quite small, which means that there were few, if any, "pure" pixels on the smaller targets. This effect was exacerbated by the fact that the lens on our camera was not achromatic in the SWIR, which caused a difference in the focus between the two bands. When the spectral content of a given pixel is mixed between target and

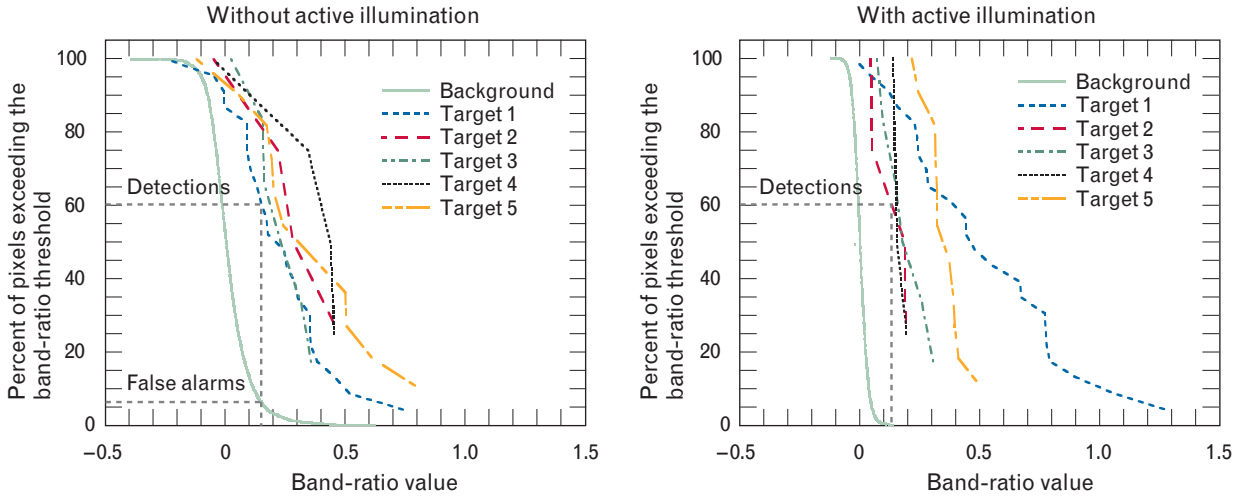

FIGURE 14. Cumulative probability distribution curves for each target and the background in a scene imaged (a) without active illumination and (b) with active illumination. The cumulative probability distributions for the active illumination show greater separability between the targets and the background.

background, the band ratio will be smaller. Given these factors, the performance increase due to active illumination could potentially be greater.

Summary

Multispectral and hyperspectral imaging continues to grow and evolve as a powerful remote sensing tool. But relying on the sun for illumination introduces an additional source of uncertainty that can impact the opportunities for collecting data as well as the utility of the data. Controlling the illumination source can reduce some of these uncertainties and also offer additional benefits. Tactical applications especially will benefit from the ability to operate at night, and having the illumination source coincident with the imager reduces shadowing within the target scene. In both laboratory and outdoor measurements we have shown that the reduced shadowing results in increased contrast and reduced false-alarm rates. Active illumination also provides the opportunity to use polarization and fluorescence features in conjunction with the spectral data to improve detection capability.

While the research summarized in this article has explored the phenomenology and demonstrated proof-of-concept approaches for active spectral imaging, the promise shown does motivate a number of more detailed follow-on questions. In particular, questions come to mind with regard to the sensitivity of active spectral imaging to the number, width, and location of spectral bands, with target detection and identification performance as quantitative metrics. Also, the performance gains from the addition of three-dimensional imaging or polarization sensitivity are areas worthy of further investigation. This additional research in developing more quantitative performance estimates and comparisons is best pursued in the context of specific target materials and detection scenarios, and, we hope, will be the subject of our future work.

Acknowledgments

This program has been very much a team effort, and we would like to acknowledge the contributions of Amy Newbury, Mrinal Iyengar, Hsiao-hua Burke, Bernadette Johnson, Bert Willard, Gary Swanson, and Herb Barclay to the work discussed.

REFERENCES

1. A.B. Gschwendtner and W.E. Keicher, "Development of Coherent Laser Radar at Lincoln Laboratory," *Linc. Lab. J* **12** (2), 2000, pp. 383–396.
2. R.G. Reeves, ed., *Manual of Remote Sensing, Vol. 1* (American Society of Photogrammetry, Falls Church, Va, 1975).
3. R.M. Heinrichs, B.F. Aull, R.M. Marino, D.G. Fouche, A.K. McIntosh, J.J. Zayhowski, T. Stephens, M.E. O'Brien, and M.A. Albota, "Three-Dimensional Laser Radar with APD Arrays," *SPIE* **4377,** 2001, pp. 106–117.
4. B. Johnson, R. Joseph, M. Nischan, A. Newbury, J. Kerekes, H. Barclay, B. Willard, and J.J. Zayhowski, "A Compact, Hyperspectral Imaging System for the Detection of Concealed Targets," *SPIE* **3710,** 1999, pp. 144–153.
5. J.J. Zayhowski, "Passively *Q*-Switched Nd:YAG Microchip Lasers and Applications," *J. Alloys Compd.* **303–304,** 24 May 2000, pp. 393–400.
6. A.B. Newbury, M. Nischan, R. Joseph, M. Iyengar, B. Willard, J. Libby, G. Swanson, B. Johnson, and H. Burke, "Detection of Manmade Objects," *SPIE* **4132,** 2000, pp. 126–135.
7. J.R. Schott, *Remote Sensing: The Image Chain Approach* (Oxford University Press, New York, 1997).
8. R. Anderson, W. Malila, B. Maxwell, and L. Reed, *IRIA State of the Art Reports, SOAR 1, Military Utility of Multispectral and Hyperspectral Sensors,* Report No. 246890-3-F, Environmental Research Institute of Michigan, Ann Arbor, Mich. (11 Nov. 1994).
9. J.D. Howe, M.A. Miller, R.V. Blumer, T.E. Petty, M.A. Stevens, D.M. Teale, and M.H. Smith, "Polarization Sensing for Target Acquisition and Mine Detection," *SPIE* **4133,** 2000, pp. 202–213.
10. A.C. Schuerger, G.A. Capelle, J.A. Di Benedetto, C. Mao, C.N. Thai, M.D. Evans, J.T. Richards, T.A. Blank, and E.C. Stryjewski, "Comparison of Two Hyperspectral Imaging and Two Laser-Induced Fluorescence Instruments for the Detection of Zinc Stress and Chlorophyll Concentration in Bahia Grass (*Paspalum Notatum* Flugge)," *Remote Sens. Environ.* **84** 2003, pp. 572–578.
11. M.L. Nischan, A.B. Newbury, R. Joseph, M. Iyengar, B. Willard, G. Swanson, J. Libby, B. Johnson, and H.-H. Burke, "Active Hyperspectral Imaging," *SPIE* **4312,** 2000, pp. 107–117.

MELISSA L. NISCHAN
is an associate staff member in the Sensor Technology and System Applications group. She helped develop and field test active hyperspectral/multispectral sensors, and characterized the performance of various detector and laser systems. She also developed a non-line-of-sight ultraviolet communications test bed and software for distributed networking applications. Currently, Melissa works on water monitoring systems for biodefense. She joined the Laboratory in 1996, after graduating from the University of Massachusetts, Amherst, with an M.S. degree in astronomy. She also holds a B.A. degree in physics from Franklin and Marshall College in Lancaster, Pennsylvania. She is a member of Sigma Pi Sigma: the National Physics Honor Society.

ROSE M. JOSEPH
is a staff member in Biodefense Systems group, where she researches models for improved bioaerosol detection. Before joining the Laboratory in 1997, she worked on advanced color xerography for Xerox Corporation in Webster, New York. Rose earned an S.B. degree in electrical engineering from MIT and a Ph.D. degree in electrical engineering and computational electromagnetics from Northwestern University.

JUSTIN C. LIBBY
is an associate staff member in the Laser and Sensor Applications group. Upon joining the Laboratory in 2000, he worked on the wake vortex laser radar (ladar) system, collecting data on commercial aircraft as well as the V-22 Osprey, a military tiltrotor aircraft. Justin has also performed data-registration algorithm development for 3D ladar systems, as well as system design, assembly, and testing for the laser vibrometry program. For the hyperspectral imaging program, he participated in fielding the multispectral imager system and the active multispectral range imager. Justin earned B.S. and M.S. degrees in applied physics from Cornell University.

JOHN P. KEREKES
is a staff member in the Sensor Technology and System Applications group. His primary area of research has been the development of remote sensing system-performance models for geophysical parameter retrieval and object detection and discrimination applications. After joining Lincoln Laboratory in 1989, he worked on performance analyses for ballistic missile discrimination problems. He then developed analysis models supporting weather-satellite instrument development. In particular, he developed models to study the accuracy of proposed sensor systems in retrieving the atmospheric vertical temperature and water-vapor profiles. Recently, he has developed modeling approaches for the prediction of the system performance of hyperspectral imaging systems. He is a senior member of the Institute of Electrical and Electronic Engineers (IEEE), and a member of the American Geophysical Society, the American Meteorological Society, and the American Society for Photogrammetry and Remote Sensing. He is an associate editor of the *IEEE Transactions on Geoscience and Remote Sensing*, and chairs the Boston Chapter of the IEEE Geoscience and Remote Sensing Society. He received his B.S., M.S., and Ph.D. degrees in electrical engineering from Purdue University.